

Space Weather®



RESEARCH ARTICLE

10.1029/2023SW003438

Key Points:

- Six satellites with in situ probe provide unprecedented coverage of equatorial region for reliable detection of equatorial plasma bubbles (EPBs)
- We developed new approaches for construction the global maps of EPBs geolocations
- Results agreed well with independent observations and climatological characteristics of plasma bubbles occurrence

Correspondence to:

I. Zakharenkova, irinaz@ucar.edu

Citation:

Zakharenkova, I., Cherniak, I., Braun, J. J., & Wu, Q. (2023). Global maps of equatorial plasma bubbles depletions based on FORMOSAT-7/COSMIC-2 ion velocity meter plasma density observations. *Space Weather*, 21, e2023SW003438. https://doi.org/10.1029/2023SW003438

Received 18 JAN 2023 Accepted 28 APR 2023

Author Contributions:

Conceptualization: Irina Zakharenkova, Iurii Cherniak, John J. Braun, Qian Wu Data curation: Irina Zakharenkova Formal analysis: Irina Zakharenkova, Iurii Cherniak

Funding acquisition: John J. Braun Investigation: Irina Zakharenkova, Iurii Cherniak, John J. Braun, Qian Wu Methodology: Irina Zakharenkova, Iurii Cherniak

Project Administration: John J. Braun Software: Irina Zakharenkova Validation: Irina Zakharenkova, Iurii Cherniak, Qian Wu Visualization: Irina Zakharenkova Writing – original draft: Irina Zakharenkova, Iurii Cherniak, John J. Braun, Qian Wu

© 2023. The Authors.

This is an open access article under the terms of the Creative Commons Attribution-NonCommercial-NoDerivs License, which permits use and distribution in any medium, provided the original work is properly cited, the use is non-commercial and no modifications or adaptations are made.

Global Maps of Equatorial Plasma Bubbles Depletions Based on FORMOSAT-7/COSMIC-2 Ion Velocity Meter Plasma Density Observations

Irina Zakharenkova¹, Iurii Cherniak¹, John J. Braun¹, and Qian Wu^{1,2}

¹COSMIC Program Office, University Corporation for Atmospheric Research, Boulder, CO, USA, ²HAO, University Corporation for Atmospheric Research, Boulder, CO, USA

Abstract FORMOSAT-7/COSMIC-2 is the largest equatorial multi-satellite constellation of six full-size satellites to study the equatorial ionosphere. Each satellite is equipped by an ion velocity meter (IVM) instrument to provide high rate in situ plasma density observations along the low-inclined satellite orbits at ~530–550 km altitude. Six satellites provide an unprecedented dense coverage of the entire equatorial region around the globe and allow reliable detection of equatorial plasma bubbles (EPBs) and plasma density irregularities at different local times/longitudinal sectors simultaneously. We present a method for detection of EPBs in FORMOSAT-7/COSMIC-2 in situ plasma density data and construction of the global maps of EPB geolocations. The results in the form of time series and IVM-based global Bubble Maps have a great potential for both near real-time monitoring of space weather conditions and long-term statistical analysis of EPB occurrence in regional or global scales. We present first FORMOSAT-7/COSMIC-2 derived climatological characteristics of the post-sunset and post-midnight EPBs occurrence probability and their apex altitudes during a period of low solar activity. Also, we demonstrate the good performance of the FORMOSAT-7/COSMIC-2 IVM-based Bubble Maps when compared to optical images and ground-based ionosonde observations.

Plain Language Summary Recently lunched satellite mission FORMOSAT-7/COSMIC-2 represents the largest equatorial mission of six spacecrafts that fly near the equator at 550 km altitude and measures various characteristics of the Earth's ionospheric plasma. Each satellite is equipped with an instrument for contact measurements of ionospheric plasma density and plasma motions—an ion velocity meter. Six satellites operate together around the globe, and they can probe the ionosphere at different longitudes and local times simultaneously. We use FORMOSAT-7/COSMIC-2 observations for detection of equatorial plasma bubbles (EPBs)-huge plasma depletions developed after sunset over the equator. Detection of such structures is very important because of their impact on radio signals propagation. In this paper, we describe methodology on how we can detect EPBs and how to create global maps of their geolocation. The obtained results with time series of identified bubbles and global bubble maps can be used for near real-time monitoring of ionospheric depletions and for statistical analysis of their occurrence around the globe.

1. Introduction

Equatorial plasma bubbles (EPBs) represent a typical post-sunset phenomenon in the form of plasma density depletions that are observed in the equatorial ionosphere within a band of ± 15 –20° magnetic latitude (MLAT) (Kelley, 1985; Woodman & La Hoz, 1976). Post-sunset ionospheric irregularities were first observed in the 1930s (Booker & Wells, 1938) using ionosondes as the spreading in range and frequency on ionograms recording the equatorial F region echoes. This phenomenon has become known as equatorial spread F (ESF) as an EPB signature seen in ionosonde measurements. At present, EPBs are considered as quite narrow structures of depleted plasma with zonal (east–west) dimensions of ~50–250 km, but they are significantly elongated in the magnetic meridional (north–south) direction with extension over 1,000 km from the magnetic equator (Hysell, 2000; Ossakow, 1981). In altitudinal domain, EPBs cover a broad range of altitudes from the bottomside ionosphere up to above 1,000 km; the highest altitude of the depleted magnetic flux tubes above the magnetic equator is also called apex altitude of the bubble. Under quiet night-time conditions, EPBs typically drift eastward at speeds mainly within the range of 100–200 m/s (Kintner et al., 2004; Tsunoda et al., 1982).

Understanding of EPB phenomenon is highly important due to its direct effects on radio wave propagation. Ionospheric irregularities with scale sizes of meters to kilometers developing within EPB structures can severely

ZAKHARENKOVA ET AL. 1 of 16

disrupt the radio wave propagation channel by affecting both amplitude and phase of the radio signal—these disruptions are called scintillations. Scintillations occur at a broad range of frequencies. L-Band scintillation adversely impacts the trans-ionospheric communications and continuous tracking of Global Navigation Satellite System (GNSS) signals used for position, navigation, and timing services. EPBs that develop after local sunset can persist for many hours afterward and can cover a broad longitudinal range, and this space weather phenomenon is considered to be a significant threat to communication and navigation systems that operate in either space or ground environments and that rely on trans-ionospheric radio signals propagation. To understand and forecast EPB occurrence, numerous investigations were performed in the last several decades to reveal key characteristics of EPB morphology and climatology using various ground-based and satellite observations (e.g., Aarons, 1993; Abdu et al., 1983; Basu et al., 1980, 1996; Fejer & Kelley, 1980; Fejer et al., 1999; Hysell & Burcham, 2002; Kil, 2015; Makela et al., 2010; Maruyama & Matuura, 1984; Nishioka et al., 2011; Tsunoda, 1983; Valladares et al., 1996).

Considering the limited field-of-view of ground-based instruments (like ionosondes, coherent radars, all-sky cameras, GNSS receivers etc.), and the fact that the majority of the Earth's equatorial region is covered by oceans, the equatorial ionosphere has sparse global coverage from ground-based detectors. Satellites have the potential to provide continuous observations suitable for EPB detection and monitoring around the globe. Previously, continuous and long-term in situ plasma density observations have been successfully used to derive statistical characteristics of EPB occurrence on a global scale in the form of a typical seasonal/longitudinal (S/L) distribution of EPBs as detected in the datasets of the DMSP satellites (Burke et al., 2004; Gentile et al., 2006; Huang et al., 2001), the ROCSAT-1 satellite (Su et al., 2006; Kil et al., 2009), the C/NOFS satellite (Huang et al., 2014), the CHAMP satellite (Xiong et al., 2010) and of the Swarm satellites (Zakharenkova et al., 2016). Each new satellite mission equipped with in situ plasma probes can provide new insights and discoveries to support EPB research. For instance, prior to the launch of the C/NOFS satellite, EPBs were mainly considered as post-sunset phenomena. It was found out that under solar minimum conditions, EPBs regularly appear at post-midnight to dawn local times (Burke et al., 2009; de La Beaujardière et al., 2009; Gentile et al., 2011).

In April 2006, the first constellation of six small satellites—Formosa Satellite 3/Constellation Observing System for Meteorology, Ionosphere, and Climate (FormoSat-3/COSMIC-1, hereafter F3/C1)—was successfully launched into the orbit of \sim 700–800 km altitude and 72° inclination. When fully operational, F3/C1 produced 1,500–2,500 Radio Occultation (RO) soundings of the ionosphere per day, thus providing the unprecedentedly dense coverage on a global scale. The F3/C1 RO observations were also used to study the climatology of ionospheric irregularities associated with EPB development. Carter et al. (2013) investigated occurrence of equatorial F layer irregularities on the base F3/C1 S4 scintillation product for 2007–2011 years and reported EPB occurrence dependence on season/longitude, as well as impact of solar activity level for plasma irregularities probability in different longitudinal sectors and seasons. The same F3/C1 S4 scintillation product was broadly used to study altitudinal distribution of the amplitude scintillations in the ionospheric E and F regions under various conditions (e.g., Brahmanandam et al., 2012; Dymond, 2012; Liu et al., 2016). To investigate climatology of medium-scale F region ionospheric plasma irregularities, Watson and Pedatella (2018) used F3/C1 RO detrended total electron content (TEC) measurements. They analyzed periods of the solar minimum and ascending phase of the 24th solar cycle and reported seasonal occurrence patterns when high rate of ionospheric irregularities occurrence predominated in regions near to the solar terminator and altitudes ~ 300 km. Chou et al. (2020) used the similar approach (F3/C1 absolute TEC product with filtered background TEC variations) to analyze EPB climatology during the 24th solar cycle. The authors also reported strong solar dependence and correlation of longitudinal and seasonal EPB distribution patterns with the angle between solar terminator and geomagnetic field lines over the magnetic equator. Cherniak et al. (2019) used the combination of F3/C1 RO electron density profiles and S4 scintillation product together with in situ plasma probe observations from C/NOFS, Swarm, and DMSP satellites to characterize development of the storm-induced EPBs; the authors also demonstrated the first successful application of the backpropagation geolocation technique (Sokolovskiy et al., 2002) to F3/C1 GPS data. Apart from the climatological studies of EPB occurrence, F3/C1 RO observations were used to investigate effects of plasma irregularities phenomenon on GPS RO signals and transient loss of lock probability (e.g., Yue et al., 2016).

In the present study, we propose to take full advantage of in situ plasma density observations provided by the new satellite mission FORMOSAT-7/COSMIC-2 (thereafter, F7/C2) that was launched on 25 June 2019 into a low-inclination orbit (24°). To date, the F7/C2 equatorial constellation represents largest satellite-based observational system to study the equatorial ionosphere. This six satellite constellation operates at \sim 530–550 km orbital

ZAKHARENKOVA ET AL. 2 of 16

altitude, separated by $\sim 60^{\circ}$ in longitude to provide a global and uniform observations coverage that samples the equatorial ionosphere region with multiple types of ionospheric observations. This includes limb and overhead TEC, RO electron density profiles, amplitude/phase scintillations, and in situ ion plasma densities. From the mission objectives, it is expected that the F7/C2 multi-instrumental observations will substantially contribute to a better understanding of the equatorial ionosphere morphology and future forecasting of ionospheric irregularities and radio wave scintillations that harmfully affect satellite-to-Earth communication and navigation systems.

Detection of EPB signatures in the in situ plasma density observations is strongly dependent on satellite orbit inclination. For highly inclined or polar orbiting LEO (Low Earth Orbit) satellites, each successive orbit will cross the equator approximately ~15° west in longitude, and thereby never re-sampling the same geographical area during the same day (and LT). This restricts the ability of a single, polar orbiting, satellite to provide information how EPBs evolved in time over a unique longitudinal sector. Only satellites with a low inclination orbit are capable of sampling equatorial and low latitude regions multiple times per day and can potentially encounter the same plasma depletion structure again. For example, Huang et al. (2011) reported that if a particular EPB existed for longer than 100 min (orbit period), the bubble can be detected by several successive passages of C/NOFS satellite, which had ~13° orbit inclination—that provided a possibility to analyze the generation and spatial evolution of EPBs in time, in particular formation of broad plasma depletions using C/NOFS in situ data. For the F7/C2 mission, the configuration of six satellites with identical observational capabilities that are distributed evenly around the globe in a ~24° inclined orbit provides an opportunity to encounter plasma depletion structures with a sampling rate that is much faster than any single satellite could provide. Figure 1a shows an example of 1 day orbit coverage by six F7/C2 satellites—having each satellite with ~14 orbits per day, F7/C2 provides sampling of low latitude region with unprecedented daily coverage. Figure 1b shows an example of orbit track location during 1 hour (00-01 UT on 5 January 2022); one can see that with all six satellites, each longitudinal sector is crossed by at least 2-3 satellites during a one-hour period, of course, with different distance from the magnetic equator. Figure 1c illustrates in situ ion density measurements provided by the ion velocity meter (IVM) instrument along corresponding orbit tracks for different F7/C2 satellites shown in Figure 1b. Here, in the local post-sunset period over western South America, two F7/C2 satellites, C2E3 and C2E4 (shown by red and blue color, respectively), encountered near simultaneously deep plasma density depletions over that area. The C2E4 satellite's orbit projection in the American-Atlantic sector (80°W-15°E) was closely aligned with the magnetic equator, making it possible to identify multiple EPBs over South America that had already reached the satellite orbit altitude (~550 km) and stretched out for more than 40° in the longitudinal range. Examination of the observations from the satellites, whose overpasses located at some distance from the magnetic equator, can help us to determine the latitudinal extension of EPBs from the magnetic equator into different hemispheres. Analysis of the observations in the magnetic coordinates can provide some clue if some simultaneously identified depletions correspond to possibly the same EPB structure that elongated near the same magnetic meridian and was crossed by two different satellites in a short period of time. This example clearly demonstrates enormous advantages of utilizing the F7/C2 in situ observations for EPB investigations. The objective of the present paper is to present fundamentals of the developed algorithm for EPB detection in F7/C2 in situ plasma density data and construction of the global maps of EPB geolocations, as well as their performance evaluation.

2. Data Set and Methodology of the IVM-Based Bubble Map

The processing chain of the F7/C2 IVM-based Bubble Map Algorithm consists of multiple steps (Figure 2): (a) analysis of raw ion density data; (b) establishing indices which can identify the occurrence of plasma density irregularities in the in situ density measurements; (c) setting thresholds; (d) two-dimensional mapping techniques. Each step will be discussed in detail below.

2.1. F7/C2 IVM Ion Density Measurements

To date, the F7/C2 is the largest equatorial multi-satellite constellation of six full-size satellites to study the equatorial ionosphere. The F7/C2 payload includes an IVM instrument to provide measurements of the ion drift, density, and major ion composition along the satellite orbit altitude at \sim 530–550 km. The IVM instrument consists of two planar sensors—a Retarding Potential Analyzer and an Ion Drift Meter. Both sensors are utilized to derive currents and voltages for calculating the total ion density, composition, temperature, and drift through a least-square fitting procedure (Heelis et al., 2017). The F7/C2 IVM ion density can be obtained in the level 2

ZAKHARENKOVA ET AL. 3 of 16

15427990, 2023, 5, Downloaded from https://agupubs.onlinelibrary.viley.com/doi/10.1029/2023SW003438, Wiley Online Library on [31/07/2023]. See the Terms and Conditions (https://onlinelibrary.wiley.com/terms-and-conditions) on Wiley Online Library for rules of use. OA articles are governed

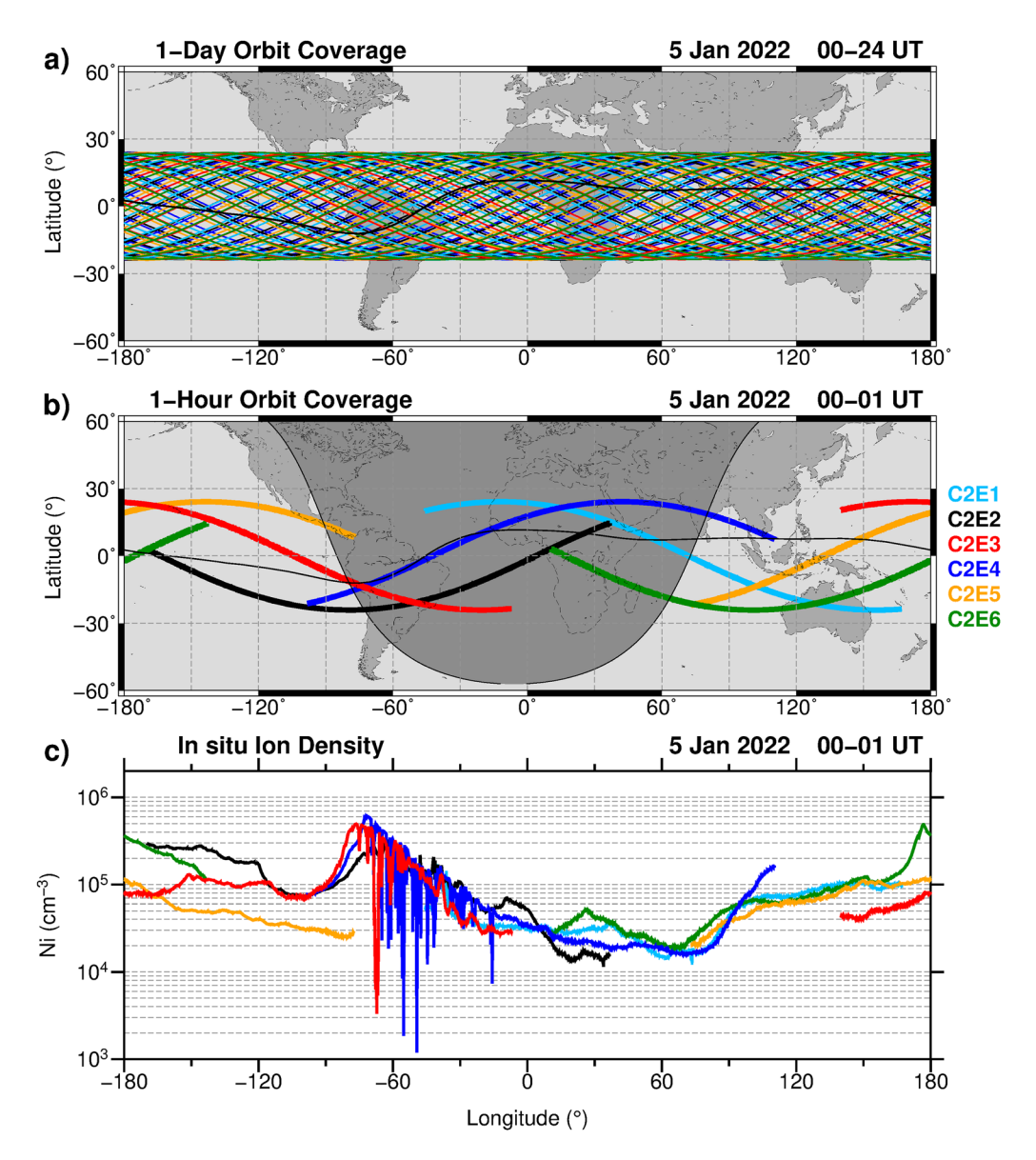


Figure 1. Example of F7/C2 orbit coverage by six satellites for the equatorial region during (a) 24 hr and (b) 1 hour; (c) ion velocity meter in situ ion density along corresponding 1-hr tracks for different F7/C2 satellites (indicated by color).

product "ivmLv2" file in the COSMIC Data Analysis and Archive Center (CDAAC, http://cdaac-www.cosmic.ucar.edu) database. In this study, we used total ion density (Ni) provided with 1 Hz from six F7/C2 satellites and calibrated using F7/C2 TGRS observations (Wu et al., 2022) to analyze the occurrence of EPBs on a global scale.

2.2. Bubble Index

To identify the occurrence of plasma density irregularities in the in situ density measurements, we used a "Bubble Index" parameter, σ , that represents relative standard deviation of ion density (Ni) variation in logarithmic scale divided by the mean of ion density in logarithmic scale (Equations 1 and 2). A similar approach was successfully utilized for in situ plasma density measurements onboard AE-E (Kil & Heelis, 1998), ROCSAT-1 (Su et al., 2006), and C/NOFS (Huang et al., 2014) satellites to retrieve climatological features of EPBs occurrence. The only difference is that in these earlier studies the running mean had a 10-s window, here we used a 15-s window. Considering that satellites move with ~7 km/s, the 15-s window corresponds to ~100 km or ~1° coverage in the longitudinal range to calculate that mean.

ZAKHARENKOVA ET AL. 4 of 16

15427390, 2023, 5, Downloaded from https://agupubs.onlinelibrary.wiley.com/doi/10.1029/2023SW003438, Wiley Online Library on [31/07/2023]. See the Terms and Conditions (https://agupubs.onlinelibrary.wiley.com/doi/10.1029/2023SW003438, Wiley Online Library on [31/07/2023]. See the Terms and Conditions (https://agupubs.onlinelibrary.wiley.com/doi/10.1029/2023SW003438, Wiley Online Library on [31/07/2023]. See the Terms and Conditions (https://agupubs.onlinelibrary.wiley.com/doi/10.1029/2023SW003438, Wiley Online Library on [31/07/2023]. See the Terms and Conditions (https://agupubs.onlinelibrary.wiley.com/doi/10.1029/2023SW003438, Wiley Online Library on [31/07/2023]. See the Terms and Conditions (https://agupubs.com/doi/10.1029/2023SW003438, Wiley.com/doi/10.1029/2023SW003438, Wiley.com/doi/10.1029/2023SW003438,

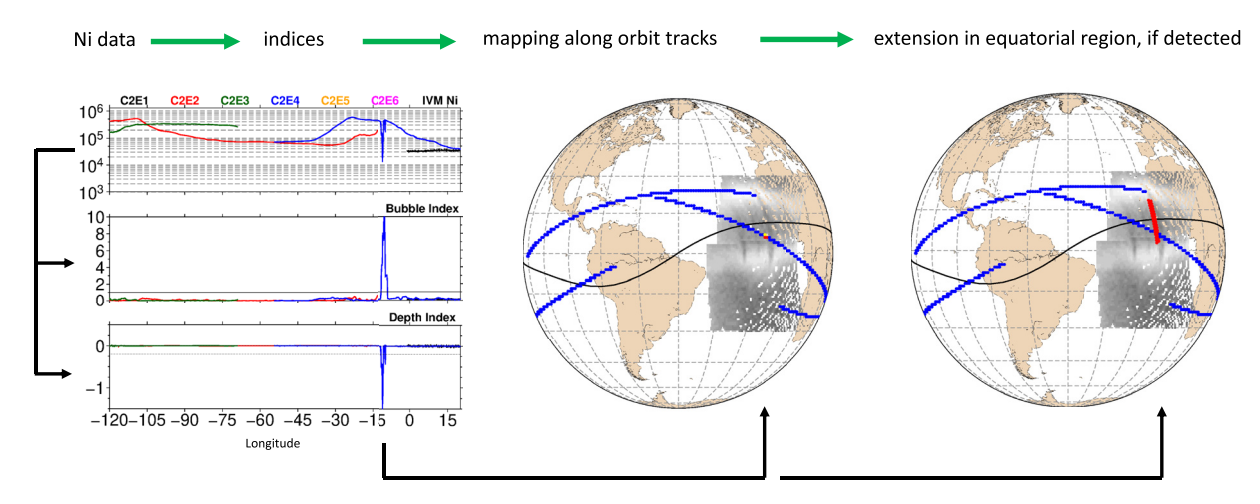


Figure 2. General scheme of the F7/C2 IVM-based Bubble Map Algorithm.

$$\sigma = \frac{\text{std}}{\text{mean}} \cdot 100 = \frac{\sqrt{\sum_{k=1}^{n} |\log_{10}(Ni_k) - \text{mean}|^2}}{\sum_{k=1}^{n} |\log_{10}(Ni_k) - \text{mean}|^2} \cdot 100$$

mean =
$$\frac{\sum_{k=1}^{n} \log_{10}(Ni_k)}{n}$$
, n = 15

2.3. Depth Index

We should note that the Bubble Index, described above, represents the relative standard deviation of ion density (Ni) variations, and it is very sensitive to different types of plasma density fluctuations and gradients that are frequently present in the in situ plasma density measurements in the equatorial region. That is why its solo application can be not enough and it is typically used together with other parameters, constrains or together with a low-pass filtration (e.g., over 200–400 s). For our investigation, we propose to use an additional parameter "Depth Index" to determine whether the plasma density irregularity defined by the Bubble Index σ is indeed plasma density depletion and how deep this depletion should be to satisfy our criterion of the reliable plasma bubble. For that purpose, we need to determine appropriately the trend in the data curve that excludes most signatures of plasma density depletion—a sort of upper envelope curve for the Ni data variation. Results of simple application of polynomial fit or moving average as detrending/smoothing techniques are typically affected by the presence of strong plasma density depletions, especially if they are not isolated ones but occur over a broader longitudinal area like trains of consecutive depletions. We use the advanced data detrending algorithm "Rolling Barrel Technique" proposed by Pradipta et al. (2015). This algorithm is a mechanical analogy of rolling a cylindrical barrel on a rough uneven surface—with a sufficiently large radius, and this imaginary barrel will roll over the depletions and will not fall down into the valley/depletion areas such allow to trace the upper envelope of the overall data variation in a more precise way.

If the IVM Ni data is considered as time series (x, y) where x is time (in seconds), and y is Ni value in logarithmic scale, then the barrel rolls forward from one contact point to the next contact point that would be the one with the smallest angular distance δ with respect to the leading edge of the barrel. So, the idea is to find if the next point exists within $[x_0; x_0 + 2R_0]$ interval, which is the $2R_0$ circle where R_0 is the barrel radius, where angular distance δ (Equation 3) is minimal:

$$\delta = \sin^{-1} \left[\frac{\sqrt{(\Delta x)^2 + (\Delta y)^2}}{2R_0} \right] - \tan^{-1} \left[\frac{\Delta y}{\Delta x} \right]$$
 (3)

ZAKHARENKOVA ET AL. 5 of 16

15427390, 2023, 5, Downloaded from https://agupubs.onlinelibrary.wiley.com/doi/10.1029/2023SW003438, Wiley Online Library on [31/07/2023]. See the Terms and Conditions (https://onlinelibrary.wiley.com/doi/10.1029/2023SW003438, Wiley Online Library on [31/07/2023]. See the Terms and Conditions (https://onlinelibrary.wiley.com/doi/10.1029/2023SW003438, Wiley Online Library on [31/07/2023]. See the Terms and Conditions (https://onlinelibrary.wiley.com/doi/10.1029/2023SW003438, Wiley Online Library on [31/07/2023]. See the Terms and Conditions (https://onlinelibrary.wiley.com/doi/10.1029/2023SW003438, Wiley Online Library on [31/07/2023]. See the Terms and Conditions (https://onlinelibrary.wiley.com/doi/10.1029/2023SW003438, Wiley Online Library.wiley.com/doi/10.1029/2023SW003438, Wiley Online Library.wiley.wiley.com/doi/10.1029/2023SW003438, Wiley Online Library.wiley.wiley.wiley.com/doi/10.1029/2023SW003438, Wiley Online Library.wiley.wiley.wiley.wiley.wiley.wiley.wiley.wiley.wiley.wiley.wiley.wiley.wiley.wiley.wiley.wiley.wiley.wiley.wiley.wiley.wiley.wiley.wiley.wiley.wiley.wiley.wiley.wiley.wiley.wiley.wiley.wiley.wiley.wiley.wiley.wiley.wiley.wiley.wiley.wiley.wiley.wiley.wiley.wiley.wiley.wiley.wiley.wiley.wiley.wiley.wiley.w

ons) on Wiley Online Library for rules of use; OA articles are governed by the applicable Creative Commons License

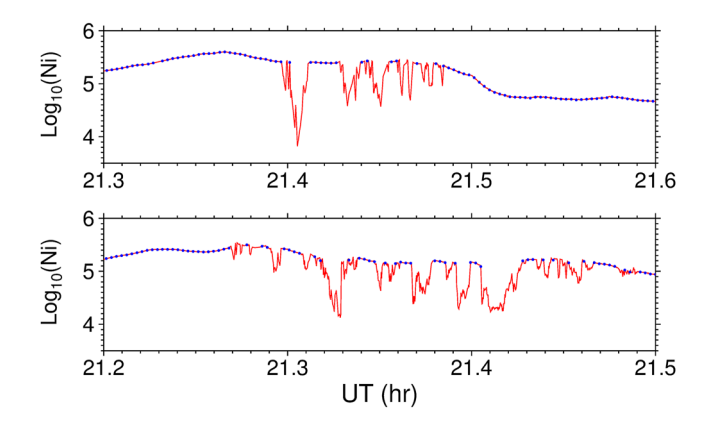


Figure 3. Two examples of Rolling Barrel Technique application to F7/C2 ion velocity meter (IVM) Ni data from C2E1 satellite in 30 March 2021 (top panel) and from C2E3 satellite in 12 March 2021 (bottom panel). Red curve—IVM Ni data in a logarithmic scale, blue dots - "barrel-roll curve," points selected after Rolling Barrel Technique application.

The resulting curve traced by all the contact points is called the "barrel-roll curve"; this curve should exclude depletions with length scale less than $2R_0$ in the time series. Figure 3 shows examples of the Rolling Barrel Technique application to F7/C2 IVM ion density data, and illustrates how the upper envelope excludes the majority of the registered plasma density depletions. This upper envelope allows for a more straightforward method to infer an accurate overall trend in ion density. To close the gaps, we apply a linear interpolation between selected points of the barrel-roll curve to retrieve curve with 1-s resolution, and then we use a running mean for all points within a window of ± 100 s to safely smooth this curve to get an accurate trend. Further, the Depth Index is calculated to represent "detrended" Ni values as deviation of the original ion density in a logarithmic scale from the inferred trend. Threshold set for the Depth Index allows us to tune on how deep the plasma density depletion should be to qualify for our selection. One important advantage of using such Depth Index is that in cases of rapid density increases, which can lead to large values of the Bubble Index, the Depth Index will be positive, thus providing no signatures of plasma density depletion (i.e., negative deviation) and such cases will be effectively eliminated as "false" detection.

Thus, our second metrics Depth Index is based on the advanced data detrending algorithm and allows a better estimation of the plasma depletion depth in the Ni data.

2.4. Thresholds

These two configurable parameters, Bubble Index and Depth Index, allow us to tune the sensitivity of the proposed algorithm using separate metrics (thresholds) for the strength of an irregularity (Bubble Index) and overall plasma depletion (Depth Index) to determine how sensitive the algorithm should be for irregularities detection in IVM data and how deep the plasma depletions should be to be selected and which plasma density structures we can tolerate to be missed out. Here, we should also mention that there is no generally accepted definition of how large the particular index must be for the reliable detection of plasma density irregularities occurrence. For example, Huang et al. (2014) used $\sigma > 1\%$ to identify the occurrence probability of ionospheric irregularities from C/NOFS in situ data; Kil and Heelis (1998) used the threshold value $\sigma > 1\%$, and Joshi et al. (2022) chose $\sigma > 1.2\%$. In our analysis, we also set a minimal standard threshold for σ of 1% for the Bubble Index. For the Depth Index, we set a threshold of -0.25 (1/4 of the order of magnitude in logarithmic scale) as a minimal excursion of the plasma density drop to be considered significant enough. The proper plasma depletion is potentially detected if both indices exceed their thresholds simultaneously ($\sigma > 1\%$; depth < -0.25). From our analysis of long-term F7/C2 IVM ion density data set, we also found rather frequent occurrence of the particular noisiness (rapid fluctuations) in density observations in the pre-dawn hours. To exclude such cases, we adjust the thresholds of both Bubble Index and Depth Index by two times ($\sigma > 2\%$; depth < -0.5) for time intervals 03–07 MLT.

2.5. Mapping Techniques

After both indices are determined for each datapoint of the IVM Ni time series, we use a two-dimensional mapping technique where plasma density depletions or their absence in IVM data are determined as a function of geographic latitude and longitude. The first step is to construct a map based on EPBs detection along orbit tracks of all available F7/C2 satellites. For this aim, we binned all obtained data within the considered time interval into the map grid of $1.0^{\circ} \times 1.0^{\circ}$ in geographic latitude and longitude; at least 5 data points should be within a cell to be considered a non-empty one. Next, we determine grid cells with large enough number of data points exceeding both specified thresholds, representing a plausible detection of EPB. For each grid cell, the number of data points that exceeded both thresholds is counted as a percentage from the total number of points within a given cell. If this percentage is within a range of 0%–25%, then it is considered as a very low probability to detect EPB within this cell (z = 0, cell is color-coded as blue, indicating absence of EPBs). If the number of points exceeding both thresholds reaches 25%–50%, then it is considered as an elevated probability to detect EPB within this cell (z = 1, cell is color-coded as yellow, indicating an intermediate level of intensity). And if this percentage

ZAKHARENKOVA ET AL. 6 of 16

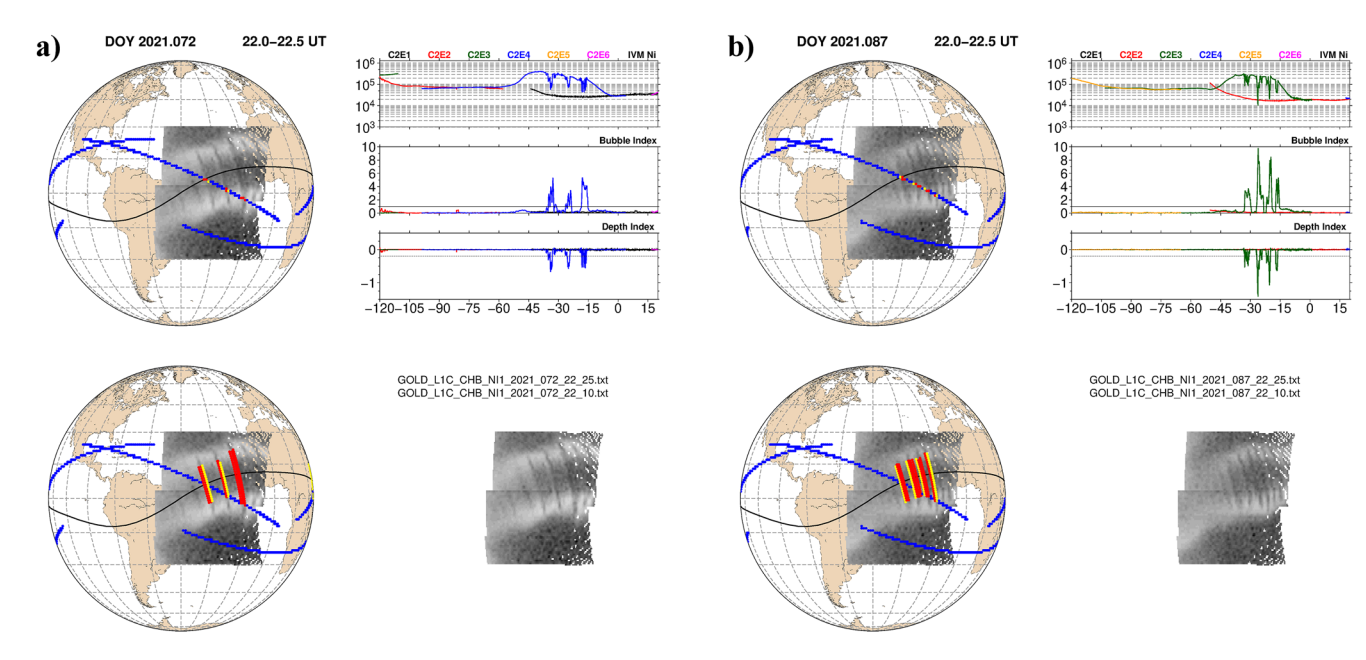


Figure 4. Examples of the IVM-based Bubble Map results in the American-Atlantic region superimposed on the GOLD UV images for 22:00-22:30 UT on (a) 13 March 2021 (DOY 072) and (b) 28 March 2021 (DOY 087).

exceeds the level of 50% for a given cell, it is considered as a high probability that detected ionospheric density irregularities within this cell correspond to EPB/depletion detection (z = 2, cell is color-coded as red indicating high intensity). In such a way, all grid cells, which have a sufficient amount of data in (that obviously corresponds to position of the satellite orbit projection into map), will be color-coded and contain an estimated probability to observe a plausible detection of EPB within a particular grid cell.

At the next step, we can estimate which latitudinal area can be potentially occupied by this particular EPB (detected plasma density depletion) and plot its position as an extension of the observed position in the magnetic north-south direction (along the magnetic field line). We should note that it is challenging to identify the actual extent of each EPB when we use only IVM in situ observations (single cross-section). That is why some assumptions about the prospective span of EPBs must be made. One way is to use a predetermined, fixed range of estimated extension for all EPBs, for instance $\pm 10^{\circ}$ or $\pm 15^{\circ}$ MLAT, as an average number from the standard EPB definition. In the present paper, two types of EPB extensions within the equatorial region were proposed to apply in the IVM-based Bubble Map algorithm—within and outside the EPBs climatological range. First, we use the following simplified empirical estimation of the climatological range of EPB apex heights determined as a function of the F10.7 solar flux index (K. Groves, private communication, 2021):

$$Apex_{clim} = 5 \cdot F_{10.7} + 325 \tag{4}$$

This empirical formula was determined on the base of in situ electron density observations onboard the C/NOFS satellite during 2008–2014, which covered both low and high solar activity periods (Joshi et al., 2022; average of two line-fits for low and high solar activity periods in Figure 4). For example, for March 2021 conditions, the monthly averaged value of the F10.7 index was ~73 SFU (SFU is Solar Flux Unit = 10^{-22} W m⁻² Hz⁻¹), the estimated value of the EPBs apex height is ~690 km that corresponds to a latitudinal extent of EPB within ±8.5° MLAT. Knowing that climatological latitudinal extent of EPBs, we can determine whether the grid cell with a plausible detection of EPB locates inside or outside of that range. If this cell locates within the climatological range of EPB, then the maximal extension (new grid cells mapped as a colored stripe along the magnetic field line) will be determined within this range. If this cell actually locates outside the climatological range, then we find the conjugate geomagnetic point and the mapped extension (colored stripe) will connect two conjugated points in both hemispheres. The apex altitude and conjugate geomagnetic points were determined using a Modified Magnetic Apex coordinate system (Richmond, 1995). Thus, this version of the Bubble Map can contain extension regions both within climatological range and outside it, depending on localization of actual IVM density observations. Two maps found in Figure 2 provide an illustration of the IVM-based Bubble Maps as

ZAKHARENKOVA ET AL. 7 of 16

(a) constructed along F7/C2 satellite orbit with a single detection of EPB (isolated red and yellow cells along the satellite orbit) and (b) the same map showing the "artificial" stretching of this EPB (red stripe) in a north-south direction to reconstruct its anticipated climatological extent (in this case, $\pm 8.5^{\circ}$ MLAT).

We should make it clear that the proposed approach of reconstructing the estimated span of EPBs is not seen as a definite, flawless way of visualizing EPBs. It is evident that the used climatological formula has certain limitations, and EPBs can actually be much larger than what was calculated. We view this as a proof of concept that the F7/C2 plasma probe data can be successfully used to detect and geolocate EPBs on a global scale, and the resulted maps can be presented in a more efficient, user-friendly way to portray bubbles as elongated structures, with the size being dependent on solar activity level. In this approach, the climatological formulation of the EPB extent can be further transformed or substituted by more advanced formulas or models.

3. Results and Discussion

The COSMIC scientific team has developed a new algorithm to determine the location of EPBs (plasma density depletions) in the F7/C2 IVM density data and to construct global maps of the identified plasma bubbles geolocations. Depending on tasks and requirements, the refreshment rate of the Bubble Map can be selected within the 30–60 min range. The results in the form of indices time series and Bubble Maps have a great potential for both near real-time monitoring of space weather conditions and long-term statistical analysis of EPB occurrence in regional or global scales.

It is important to emphasize that in situ ion density from the IVM Ni observations represents a one-dimensional transect of the ionospheric plasma at the satellite orbit altitude, so EPB signatures in the form of plasma density depletions can be detected only in cases when EPBs have already reached spacecraft altitudes (here, \sim 530–550 km). Under solar minimum conditions, not all EPBs extend to these altitudes and would therefore not be observed by the in situ plasma density sensors. With an increase of solar activity level, when EPBs rise to much higher altitudes, this technique is expected to identify more frequent detection of EPBs, in particular by satellites flying at \sim 530–550 km altitude.

Figure 4 presents two examples of the IVM-based Bubble Map results for the American-Atlantic region created in the form suitable for comparison with optical images from the Global-Scale Observations of the Limb and Disk (GOLD) mission. Launched in 2018, the NASA GOLD imager is hosted onboard a geostationary satellite over the American sector (47.5°W longitude), and it measures the Earth's far ultraviolet (UV) airglow from ~120°W to ~20°E longitude (Eastes et al., 2017). GOLD provides night-time images of atomic oxygen (O) 135.6-nm emissions; since the emission is proportional to the square of the ionospheric plasma density, the brightness is indicative of the ionospheric peak plasma density. There are two channels, A and B, that provide spectral information for either the Northern Hemisphere or the Southern Hemisphere scanning with a 15-min cadence. As of conditions in 2021, only channel B was set in night mode during 20:10-23:10 UT, imaging alternates between the Northern and Southern Hemispheres—thus, two scans from channel B are needed to construct a combined, full image of both hemispheres. When both channels were in night mode (e.g., during 23:10–00:10 UT), channel A scans the Northern Hemisphere, while channel B scans the Southern Hemisphere. GOLD observations provide an unprecedented view of the night-time ionosphere in the American-African longitudinal sector with frequent observations of EPB signatures in form of elongated plasma density depletions (Eastes et al., 2019). Thus, for that particular region, a combination of observations from two recent missions GOLD and F7/C2 can offer major benefits to the EPB research area.

Each panel of Figure 4 consists of several plots showing raw in situ Ni observations along several F7/C2 satellites available in that region and corresponding calculated results for the Bubble Index and Depth Index, and two examples of the IVM-based Bubble Maps, one with detection results along the satellites orbits and the second one with bubbles extension along the meridional plane; the IVM-based maps are overplotted above the GOLD UV images for that period of time (clear image of two north and south scans combined with details on the input file info are plotted in the bottom right corner). The two examples provided in this figure correspond to the same time interval (22:00–22:30 UT) but for two different days in March 2021. For 13 March 2021 (Figure 4a), the GOLD scans clearly reveal several regions with plasma density depletions (seen on images as an absence of emission in the form of dark narrow stripes between two brighter bands of the north/south crests of the equatorial ionization anomaly). Three distinct regions can be identified having well defined inter-bubble distance. The F7/C2

ZAKHARENKOVA ET AL. 8 of 16

satellite C2E4, transected this region during this period, and the corresponding in situ observations revealed three well-isolated depletions where both indices exceeded the established thresholds (blue curve in Figure 4a, top right). The IVM-based Bubble Map with results plotted along the satellites orbits presents the detection of these plasma density depletions (red and yellow cells) exactly over the GOLD-detected bubbles (Figure 4a, top left). The extended IVM-based Bubble Map demonstrates more explicit localization of these three plasma density depletions (Figure 4a, bottom left); two of them were extended within the climatological range and the third, most eastern one, was extended farther since observations located outside the climatological range. For the second case of 28 March 2021 (Figure 4b), the GOLD images reveal the presence of several plasma depletions with much closer longitudinal spacing than the depletions presented in Figure 4a. The example in Figure 4b shows satellite C2E3 that transected the depletion region with a similar trajectory as it was in the first case; the IVM in situ observations revealed four closely located depletions for which both indices exceeded the established thresholds (green curve in Figure 4b, top right). The extended IVM-based Bubble Map demonstrates localization of the IVM-detected plasma density depletions that coincided well with several GOLD-detected depletions on the images underneath (Figure 4b, bottom left).

Thus, geolocation of EPBs derived from the F7/C2 IVM in situ observations are found to be in a good agreement with independent GOLD UV images. We should mention that since the GOLD images represent "topside" snapshots of the ionospheric peak density as an integrated column brightness, there can be situations where GOLD can see plasma bubbles and IVM does not, meaning that EPBs do not reach the F7/C2 altitude (~530–550 km) to be registered by in situ plasma density instrument. The opposite situations can also occur when the IVM instrument detected depletions and GOLD images did not, for example, when GOLD UV emission was not quite strong and did not have enough contrast to identify the bubble depletions. But most of the time, both missions can offer complimentary observations of EPBs within the American sector. GOLD offers an excellent imaging tool for snapshots of EPBs to investigate day-to-day changes in their occurrence, EPB latitudinal extents and EPB closeness/density, but unfortunately, these GOLD night-time observations are limited by a specific time interval (20:00–00:30 UT) and for the American-African sector only.

Figure 5 presents an overview of the IVM-based Bubble Map results constructed as a global map with a 1-hr time resolution during a single day of 5 January 2022. This type of the Bubble Map representation can be used to evaluate the frequency and strength of EPBs as derived from the F7/C2 IVM in situ observations across the globe. For convenience, the maps also show the position of solar terminator and night-time conditions. Colored stripes with EPB detection had yellow and red colors corresponding to intermediate and high level of intensity of EPBs detected in IVM in situ data, respectively. First map corresponding to 00-01 UT on 5 January 2021 shows the presence of a train of detected depletions from the mid-part of South America till the west coast of Africa. The next map for 01-02 UT shows more numerous and dense localization of the IVM-detected EPBs concentrated over South America, as well as a single isolated depletion detected over the west coast of South America $(\sim75^{\circ}\text{W})$ and several depletions still detectable in the Atlantic Ocean $(\sim30^{\circ}\text{W})$. For the next several hours, one can see an intensification of plasma bubbles occurrence with multiple, back-to-back detections registered from the west coast till mid part of South America. Later on, trains of IVM-detected EPBs progressively shifted toward the Pacific Ocean; for example, at 09-10 UT, the very dense concentration of EPBs covered a broad longitudinal range from ~130°W in the Pacific Ocean till the west coast of South America (~75°W). During 10–13 UT, only several isolated depletions persisted until pre-dawn hours within that sector to be detected by satellites with trajectories close enough to the magnetic equator. For that particular day, the IVM observations did not detect an occurrence of intense plasma density depletions in the night-time conditions in other longitudinal sectors. At the last map of the day for 23-24 UT, two well-isolated geolocations with plasma depletions were detected over the east coast of South America.

Figure 6 shows a sequence of ionograms recorded during 00–11 UT on 5 January 2022 by two digisondes SaoLuis and Jicamarca that locate close to the magnetic equator at the east and west coasts of South America, respectively. As mentioned in introduction, the ionosondes observations have been used for decades for the detection of equatorial spread-F (ESF) associated with EPB occurrence overhead the ionosonde location. The digisondes provide digital ionogram records, which show variations of the virtual height (h') of reflection from the ionospheric layers as a function of the radio frequency in MHz (Huang & Reinisch, 1996). For the SaoLuis digisonde located in Brazil at eastern South America (Figure 6a), the first ionogram at 00:00 UT (~21 LT) on 5 January 2022 shows the presence of spread-F echoes at altitudes of the F2 layer peak, as well as above 500 km. Actually, the intense spread-F conditions were registered at SaoLuis starting from ~22 UT (~19 LT) on 4 January 2022

ZAKHARENKOVA ET AL. 9 of 16

15427390, 2023, 5, Downloaded from https://agupubs. onlinelibrary.wiley.com/doi/10.1029/2023SW003438, Wiley Online Library on [31/07/2023]. See the Terms and Conditions (https://onlinelibrary.wiley.com/terms-and-conditions) on Wiley Online Library for rules of use; OA articles are governed by the applicable Creative Commons Licensea

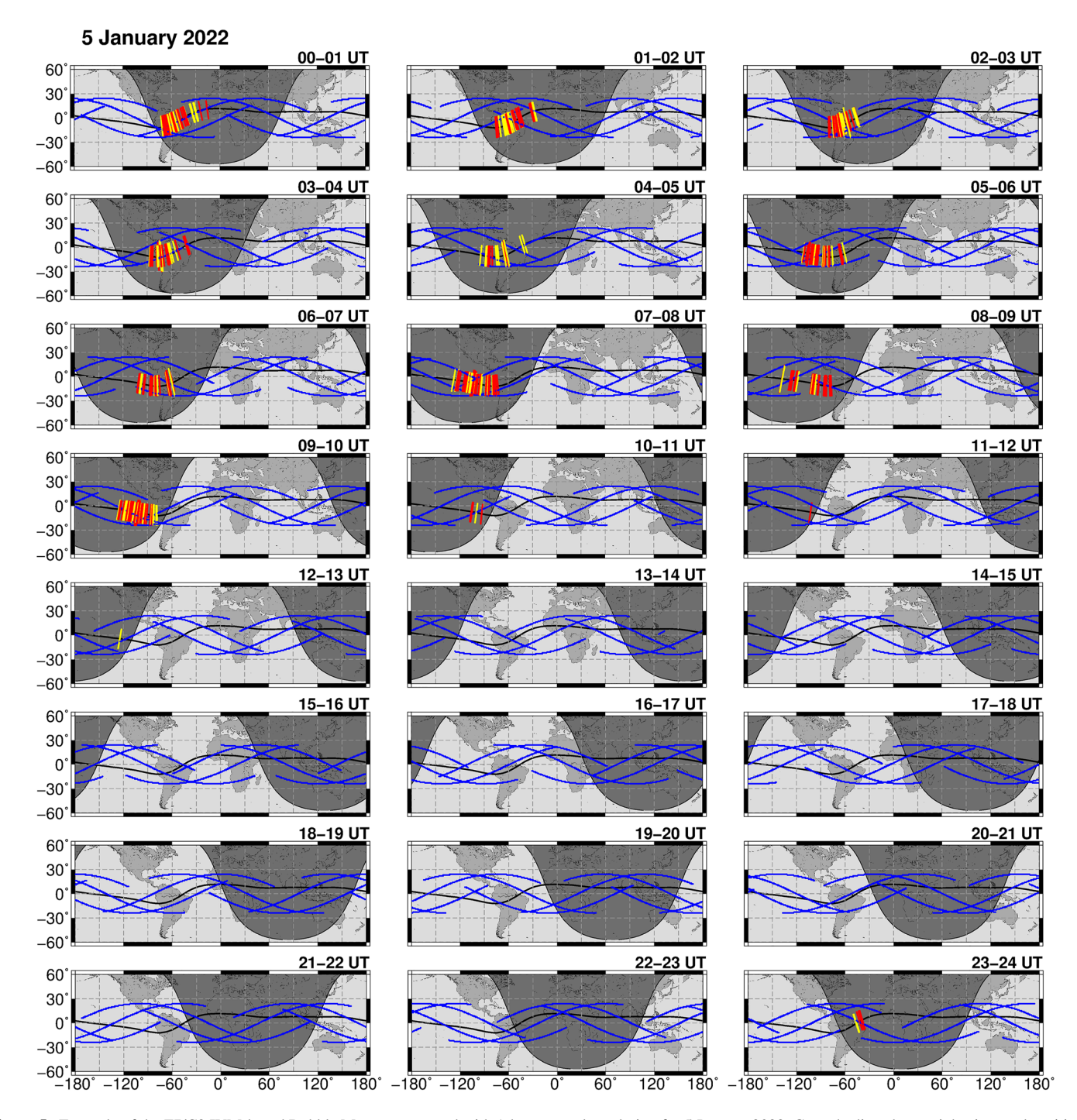


Figure 5. Example of the F7/C2 IVM-based Bubble Maps constructed with 1-hr temporal resolution for 5 January 2022. Gray shading shows night-time and position of solar terminator, thick black line shows the magnetic equator. Blue sectors show satellite locations with absence of EPBs; yellow color depicts an intermediate level of equatorial plasma bubble (EPB) activity and red color corresponds to high intensity of EPBs as detected in ion velocity meter Ni data.

(these ionograms not shown here). Near 01 UT, there was a short period when spread-F echoes slightly decreased and the ionograms become clear enough to identify ordinary (O—mode polarization) and extraordinary (X—mode) traces of the F2 layer. Then spread-F increased, and all ionograms were affected until ~05 UT on 5 January 2022. The occurrence of the bubble depletions as derived from the IVM in situ observations over that region of eastern South America (Figure 5) was quite in a good agreement with those observations of spread-F from the ground-based ionosonde—bubbles were detected in that region in IVM bubble maps from 00 UT in Figure 5 and

ZAKHARENKOVA ET AL. 10 of 16

15427390, 2023, 5, Downloaded from https://agupubs. online library.viley.com/doi/10.1029/2023SW003438, Wiley Online Library on [31/07/2023]. See the Terms and Conditions (https://onlinelibrary.wiley.com/terms-and-conditions) on Wiley Online Library for rules of use; OA articles are governed by the applicable Creative Comm

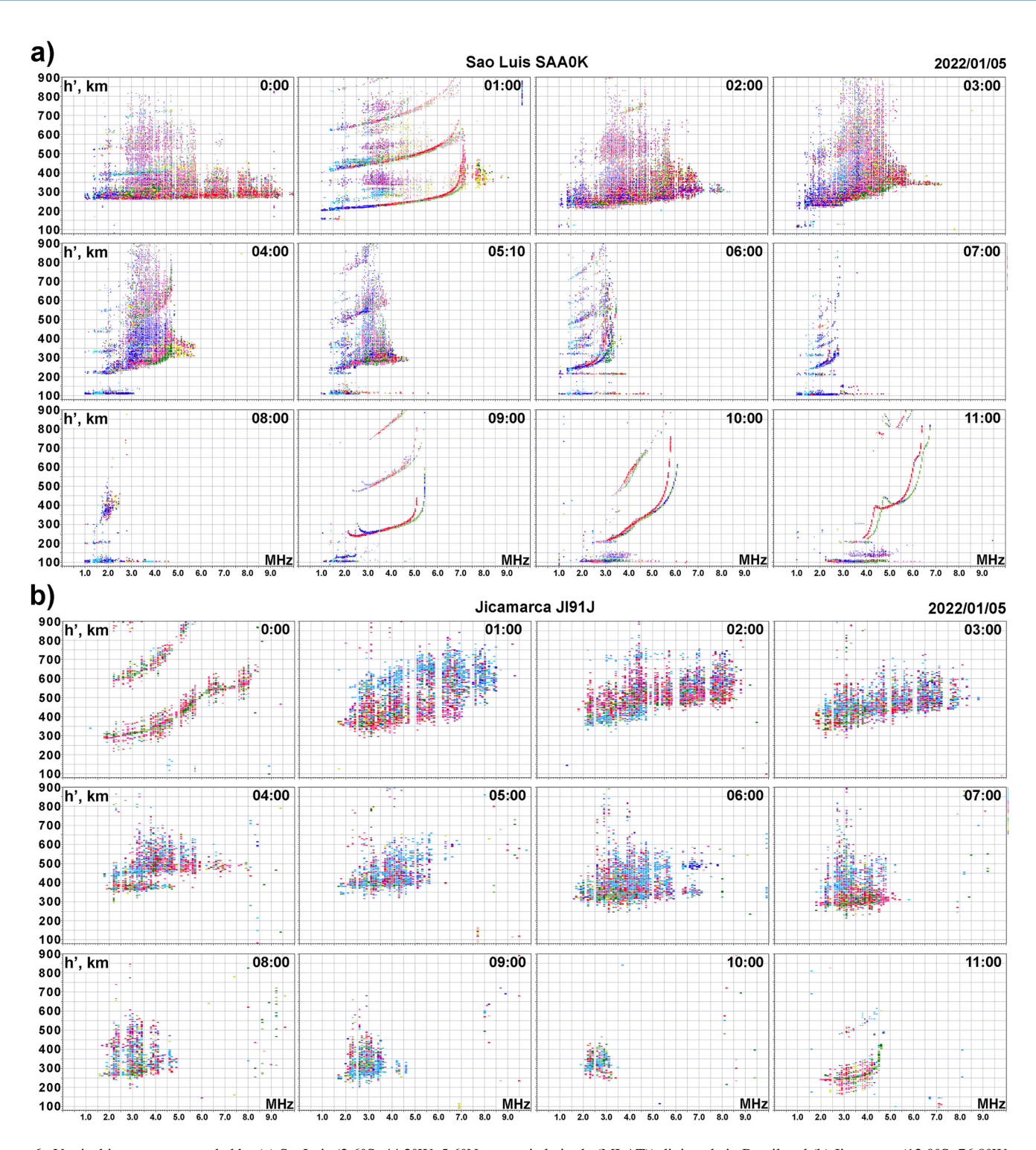


Figure 6. Vertical ionograms recorded by (a) SaoLuis (2.6°S; 44.2°W; 5.6°N magnetic latitude (MLAT)) digisonde in Brazil and (b) Jicamarca (12.0°S; 76.8°W; 2.6°S MLAT) digisonde in Peru during 00–11 UT on 5 January 2022. The O-mode polarization is shown by red trace, the X-mode—by green trace, and diffuse echoes correspond to spread-F conditions.

they have some spacing between them, the last map where depletions were detected here corresponds to 04–05 UT, similar to latest registration in the ionograms the spread-F echoes at altitudes above 500 km (to be seen by overpassing satellite too). For the Jicamarca digisonde (76.8°W in longitude) located at western South America, spread-F echoes were registered starting from ~01 UT until ~10 UT on 5 January 2022 (Figure 6b)—that is in

ZAKHARENKOVA ET AL. 11 of 16

15427390, 2023, 5, Downloaded from https://agupubs.onlinelibrary.wiley.com/doi/10.1029/2023SW003438, Wiley Online Library on [31/07/2023]. See the Terms and Condit

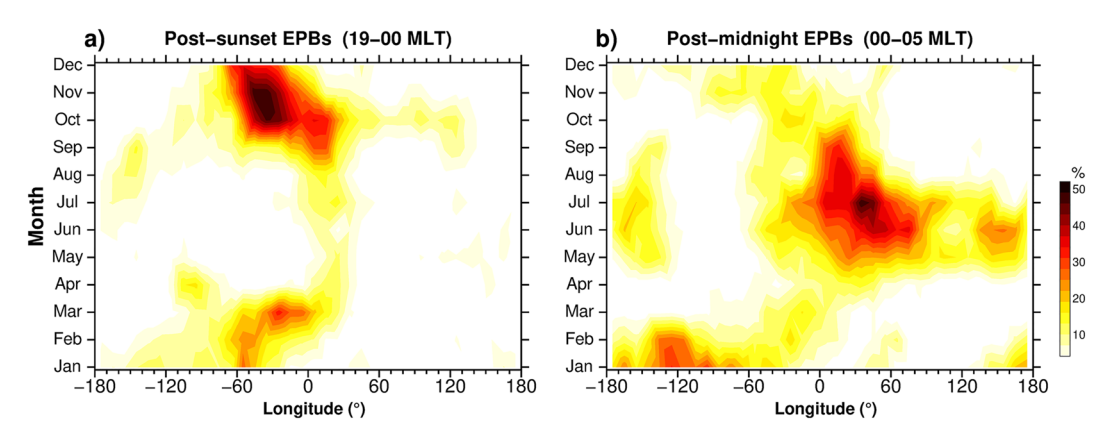


Figure 7. The longitude-month distribution of occurrence probability of (a) post-sunset and (b) post-midnight equatorial plasma bubbles detected in F7/C2 ion velocity meter measurements during the year 2021. Bins are per month and 10° longitude.

a total agreement with the time period when EPBs were detected over western South America in the IVM-based Bubble Map results, first registration corresponded to the map for 01–02 UT and the latest one was for 09–10 UT (Figure 5). Thus, spread-F observations from two distant equatorial ionosondes appear to confirm that times and specific locations of EPBs detected with F7/C2 IVM in situ observations are consistent with independent ground-based observations.

We should emphasize that with such an excellent orbit coverage (\sim 14 orbits per satellite per day) of the entire equatorial region, F7/C2 in situ plasma density observations provide us a great opportunity to study different features of EPB occurrence from a statistical point of view. We used the obtained data set of EPBs detected in F7/C2 IVM data to demonstrate climatological distribution of EPBs in the form of season-versus-longitude maps of EPB occurrence rates. To calculate EPB occurrence probability, we used the same approach as described in Huang et al. (2014). For that, only data within an equatorial latitudinal band of \pm 10° MLAT was utilized; the data for the entire year 2021 were binned by 10° in longitude and 1-month period, and split as well into post-sunset (19–00 MLT) and post-midnight (00–05 MLT) sectors. We calculated the total number of satellite orbits appeared over each longitudinal bin for each month and then the number of orbits that contain detection of EPBs (cases where both indices exceeded thresholds). The occurrence probability is then calculated as the percentage of satellite orbits with EPB detection over the total number of available orbits in each respective bin.

Figure 7 presents the longitude-month distribution of the occurrence probability for post-sunset and post-midnight EPBs in 2021. One can see that the occurrence pattern varies significantly for those two LT sectors. For the post-sunset EPB occurrence (Figure 7a), the highest occurrence rates were observed in the American-African longitudinal sector (80°W-30°E) during January-March and September-December periods. And this region showed the most prominent peaks in the occurrence rates when compared with any other longitudinal sectors around the globe. In this sector during May-August, the occurrence rate was very small (less than 5%) corresponding to the so called "low bubble season" in the American-Atlantic sector. The obtained features for the post-sunset EPB occurrence are in an excellent agreement with known climatological characteristics obtained from DMSP (Burke et al., 2004; Gentile et al., 2006), C/NOFS (Huang et al., 2014), and, particularly, with GRACE results for low solar activity period for a satellite that had a close to F7/C2 orbit altitude (Xiong et al., 2010). Considering two distinct maxima in Figure 7a, one can note that for fall season the EPB occurrence rates were larger (not symmetrical) to ones observed during the spring equinox period—that can be potentially explained with an increase of solar activity level from F10.7 ~73 SFU in March 2021 (level near 70 SFU was maintained since 2018 through the solar minimum period) to ~90 SFU in September 2021 and ~103 SFU in December 2021. As solar activity strengthens, occurrence and intensity of ionospheric irregularities increase. The occurrence rate pattern derived for the post-midnight EPBs (Figure 7b) differs substantially from one for the post-sunset period. First, a clear maximum occurs in the Atlantic-African longitudinal sector (30°W-70°E) during the May-August period with a peak near the June solstice, as well as some intensifications in the Asian-Pacific sectors. This feature with low rates or absence of EPBs in the post-sunset period and high occurrence rates in post-midnight is typically discussed in terms of non-dependency of these two types of EPBs—during June season under low solar

ZAKHARENKOVA ET AL. 12 of 16

1542/7390, 2023, 5, Downloaded from https://agupubs.onlinelibrary.wiley.com/doi/10.1029/2023SW003438, Wiley Online Library on [31/07/2023]. See the Terms and Conditions (https://onlinelibrary.wiley.com/ter

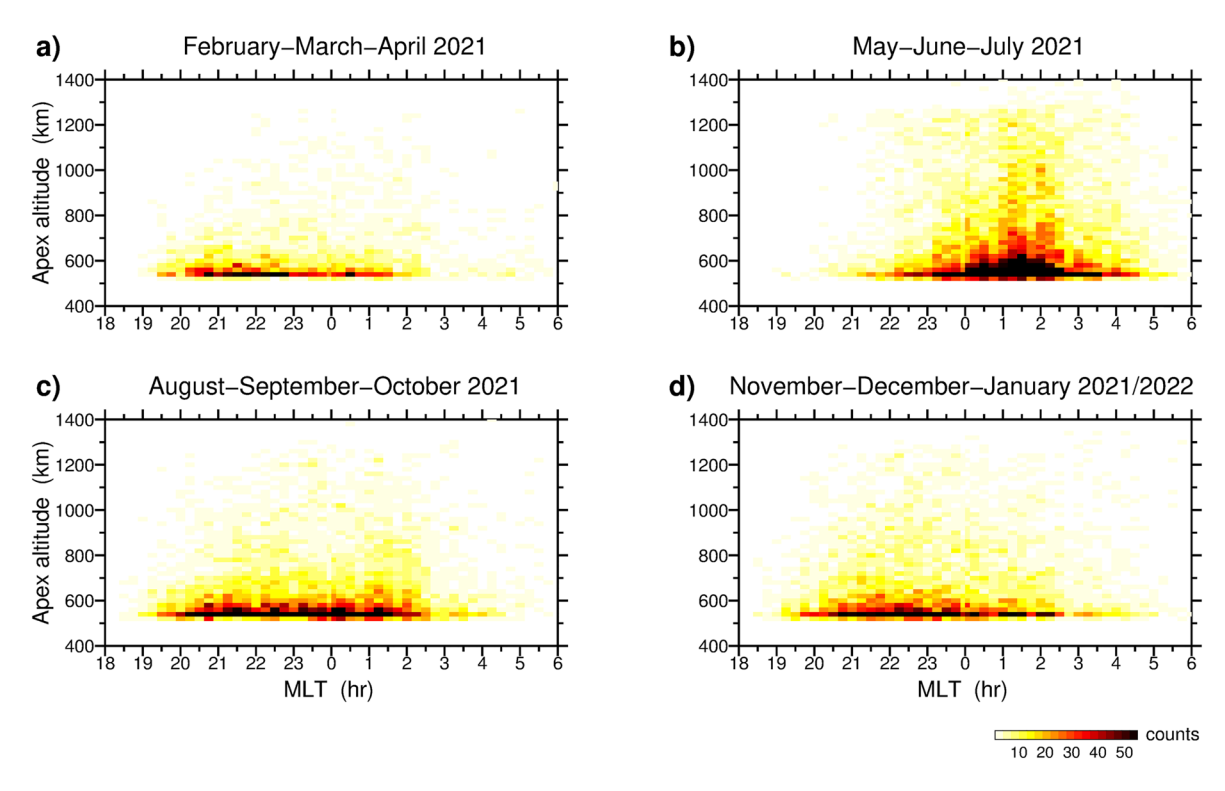


Figure 8. Statistical distribution of the apex altitude for the IVM-detected equatorial plasma bubbles as a function of magnetic local time (MLT) for (a–d) different seasons of the year 2021.

activity, the fresh EPBs are frequently generated during night in the African longitudinal sector (e.g., Yizengaw et al., 2013). Second, there is also a detected increase in the EPB occurrence rates for Pacific Ocean longitudes during January–February period. All these features are in a good agreement with results derived earlier using C/NOFS in situ observations taken during the 2008–2010 solar minimum (cf. Figure 4 in Huang et al., 2014).

Further, we investigated statistical distribution of the apex altitude of plasma density depletions as detected along the F7/C2 satellite orbits in the IVM in situ data. Figure 8 presents statistical distribution of the apex altitudes for EPBs detected in F7/C2 IVM data for different seasons centered on the solar equinoxes and solstices periods in 2021. All EPB detection data (without any restrictions on MLAT) were binned into 20 km × 15 min altitude/MLT bins that cover a various range of altitudes (500-1,400 km) and time (18-06 MLT), to describe signatures of post-sunset and post-midnight EPB occurrence. Color of each bin represents the total number of EPBs registered in that bin during the particular season (3 months period). We should emphasize that the presented results refer to the apex altitudes of the flux tubes intersected by the F7/C2 satellites, not the real apex height of EPBs. For instance, if a satellite encountered depletions in IVM density near 3°MLAT, the apex altitude will be calculated for a flux tube that has a footprint at that spot (3°MLAT), though the real bubble size could be much bigger, but not able to be determined solely from IVM observations. During the March equinox season (Figure 8a), the EPBs detected by the F7/C2 IVM in situ observations were mostly concentrated near the altitude of the satellite's orbit, as these detections were mainly located very close to the geomagnetic equator. The average apex altitude was estimated as \sim 616 \pm 106 km and \sim 650 \pm 145 km for post-sunset and post-midnight EPBs, respectively. At the second part of the year 2021 (Figures 8c and 8d), one can see some increase in the number of detected EPBs per bins at altitudes of 500-600 km, which can be probably attributed to the mentioned increase in the solar activity level during this year. For the September equinox season (Figure 8c), the average apex altitude was estimated as \sim 645 \pm 140 km and \sim 660 \pm 150 km for post-sunset and post-midnight EPBs, respectively. For the June solstice season (Figure 8b), we found that EPBs occurred predominantly in the post-midnight period and in general with much higher apex altitudes compared with ones in the pre-midnight sector for this season and other seasons as well. Most of post-midnight EPBs (~85%) occurred between 00 and 03 MLT. The average apex altitude for detected post-midnight EPBs was $\sim 706 \pm 197$ km. These features with intensification of EPB occurrence in the post-midnight sector during

ZAKHARENKOVA ET AL. 13 of 16

the June solstice season corresponded to the signatures found in the seasonal/longitudinal plot of the occurrence probability pattern (Figure 7b). The physical mechanisms for post-midnight EPBs are still the open questions. They are considered to be separated from the typical post-sunset phenomenon, so these EPBs are freshly generated later in the night. One of the discussed physical mechanisms is gravity wave seeding (e.g., Tsunoda et al., 2010) or an increase of the RT instability growth rate due to upward drift of the plasma with potential connection to the increased sporadic E occurrence (as a source of increased eastward electric fields) in June season (Yizengaw et al., 2013). The observed differences in altitudes between post-sunset and post-midnight EPBs can be related to the local time variation of the ambient plasma density (Huang et al., 2014). The ambient plasma density is high in the evening sector and decreases with local time at night. The density perturbations are small in the regions with high ambient density, but become large in the regions with low ambient density—so freshly developed post-midnight EPBs can rise to higher altitudes under conditions of low ambient density in the night-time equatorial ionosphere.

4. Summary

The results can be summarized as follows:

- 1. We presented a new approach for detection, geolocation, and mapping of plasma density depletions associated with EPB development i.e., based on the F7/C2 IVM in situ plasma density observations.
- The IVM-based Bubble Maps performance was assessed by comparison with the GOLD optical images over night-time ionosphere in the American-African longitudinal sector. Our results show that the EPB detections derived from the F7/C2 IVM in situ observations agree well with the depletion signatures seen in the GOLD UV observations.
- 3. Intense ionospheric irregularities were confirmed to be in the same places as the IVM-based EPB detections by the equatorial ionosondes from two far away locations. These ionosondes recorded spread-F echoes at the same times and specific locations with the EPBs detected by the overflying F7/C2 satellites with the IVM observations.
- 4. The long-term series of the F7/C2 IVM-based EPB detections can be used to study statistical characteristics of EPB occurrence around the world. We demonstrated that for a time of low solar activity the climatological distribution of EPBs in the form of seasonal/longitudinal maps of EPB occurrence rates based on F7/C2 IVM data reproduce well the climatological features of EPB occurrence probability, which were reported in studies based on previous satellite missions.
- 5. The obtained information on plasma density depletions detected along the F7/C2 satellite orbits in the IVM in situ data can be also used to study the EPB apex altitude characteristics on how far in altitudes above the magnetic equator the EPBs typically rise at different levels of solar activity. We found that for a period of low solar activity (2021), most of the IVM-detected bubbles were registered at ~500–700 km altitudes, rather close to the climatological range. With the upcoming solar maximum, solar activity will increase, pushing EPBs up to higher altitudes in the topside ionosphere. This will enable the six F7/C2 satellites to detect EPBs even more frequently, giving us the chance to study the global EPB occurrence and climatology with a much higher resolution and detail.

We conclude that the F7/C2 IVM-based EPB observations in the form of both time series and global IVM Bubble Maps have a great potential for both near real-time monitoring of space weather conditions and for long-term statistical analysis of EPB occurrence at a regional or global scale. It provides a novel opportunity to investigate EPB occurrence, development, and its effects on radio wave propagation and GNSS navigation performance in a whole new way.

Data Availability Statement

F7/C2 IVM density data used in this study are available at COSMIC CDAAC (UCAR COSMIC Program, 2019) and GOLD UV data are available at the GOLD Science Data Center (GOLD, 2023). Raw ionograms from DIDBase digisonde network are available through the Lowell Global Ionosphere Radio Observatory Data Center (GIRO, 2023). *Software Availability Statement*: Figures were made with the Generic Mapping Tool software version 5.4.5 (GMT, 2023; Wessel et al., 2013). Ionograms were plotted using the SAO Explorer tool for interactive ionogram scaling (SAO, 2023).

ZAKHARENKOVA ET AL. 14 of 16

15427390, 2023, 5, Downloaded from https://agupubs

online library.wiley.com/doi/10.1029/2023SW003438, Wiley Online Library on [31/07/2023]. See the Terms and Conditions (https://onlinelibrary.wiley.com

articles are governed by the applicable Creative Commons Licensu



Acknowledgments

The research is supported by the National Science Foundation under Grant 2054356 and U.S. Air Force contract FA8803-19-C-0004. We would like to thank the F7/C2 space weather cal/val team, including Paul Straus, Endawoke Yizengaw, Keith Groves, Charles Carrano, and Rod Heelis for fruitful discussions. Brazilian Ionosonde network is made available through the EMBRACE program from the National Institute for Space Research (INPE). The Jicamarca Radio Observatory is a facility of the Instituto Geofisico del Peru operated with support from the NSF AGS-1433968 through Cornell University.

References

- Aarons, J. (1993). The longitudinal morphology of equatorial F layer irregularities relevant to their occurrence. Space Science Reviews, 63(3–4), 209–243. https://doi.org/10.1007/bf00750769
- Abdu, M. A., De Medeiros, R. T., Sobral, J. H. A., & Bittencourt, J. A. (1983). Spread F plasma bubble vertical rise velocities determined from space ionosonde observations. *Journal of Geophysical Research*, 88(A11), 9197–9204. https://doi.org/10.1029/ja088ia11p09197
- Basu, S., Basu, S., Mullen, J. P., & Bushby, A. (1980). Long-term 1.5 GHz amplitude scintillation measurements at the magnetic equator. Geophysical Research Letters, 7(4), 259–262. https://doi.org/10.1029/GL007i004p00259
- Basu, S., Kudeki, E., Basu, S., Valladares, C. E., Weber, E. J., Zengingonul, H. P., et al. (1996). Scintillations, plasma drifts, and neutral winds in the equatorial ionosphere after sunset. *Journal of Geophysical Research*, 101(A12), 26795–26809. https://doi.org/10.1029/96ja00760
- Booker, H. G., & Wells, H. W. (1938). Scattering of radio waves by the F-region of the ionosphere. *Terrestrial Magnetism and Atmospheric Electricity*, 43(3), 249. https://doi.org/10.1029/te043i003p00249
- Brahmanandam, P. S., Uma, G., Liu, J. Y., Chu, Y. H., Devi, N. S. M. P. L., & Kakinami, Y. (2012). Global S4 index variations observed using FORMOSAT-3/COSMIC GPS RO technique during a solar minimum year. *Journal of Geophysical Research*, 117(9), 1–31. https://doi.org/10.1029/2012JA017966
- Burke, W. J., De La Beaujardière, O., Gentile, L. C., Hunton, D. E., Pfaff, R. F., Roddy, P. A., et al. (2009). C/NOFS observations of plasma density and electric field irregularities at post-midnight local times. *Geophysical Research Letters*, 36(18), 1–5. https://doi.org/10.1029/2009GL038879
- Burke, W. J., Gentile, L. C., Huang, C. Y., Valladares, C. E., & Su, S. Y. (2004). Longitudinal variability of equatorial plasma bubbles observed by DMSP and ROCSAT-1. *Journal of Geophysical Research*, 109(A12), A12301. https://doi.org/10.1029/2004JA010583
- Carter, B. A., Zhang, K., Norman, R., Kumar, V. V., & Kumar, S. (2013). On the occurrence of equatorial F-region irregularities during solar minimum using radio occultation measurements. *Journal of Geophysical Research: Space Physics*, 118(2), 892–904. https://doi.org/10.1002/ jora 50089
- Cherniak, I., Zakharenkova, I., & Sokolovsky, S. (2019). Multi-instrumental observation of storm-induced ionospheric plasma bubbles at equatorial and middle latitudes. *Journal of Geophysical Research: Space Physics*, 124(3), 1491–1508. https://doi.org/10.1029/2018JA026309
- Chou, M.-Y., Wu, Q., Pedatella, N. M., Cherniak, I., Schreiner, W. S., & Braun, J. (2020). Climatology of the equatorial plasma bubbles captured by FORMOSAT-3/COSMIC. *Journal of Geophysical Research: Space Physics*, 125(5), e2019JA027680. https://doi.org/10.1029/2019JA027680
- de La Beaujardière, O., Retterer, J. M., Pfaff, R. F., Roddy, P. A., Roth, C., Burke, W. J., et al. (2009). C/NOFS observations of deep plasma depletions at dawn. *Geophysical Research Letters*, 36(18), 4–7. https://doi.org/10.1029/2009GL038884
- Dymond, K. F. (2012). Global observations of L band scintillation at solar minimum made by COSMIC. Radio Science, 47(3), 1–10. https://doi.org/10.1029/2011RS004931
- Eastes, R. W., McClintock, W. E., Burns, A. G., Anderson, D. N., Andersson, L., Codrescu, M., et al. (2017). The global-scale observations of the limb and disk (GOLD) mission. Space Science Reviews, 212(1–2), 383–408. https://doi.org/10.1007/s11214-017-0392-2
- Eastes, R. W., Solomon, S. C., Daniell, R. E., Anderson, D. N., Burns, A. G., England, S. L., et al. (2019). Global-scale observations of the equatorial ionization anomaly. *Geophysical Research Letters*, 46(16), 9318–9326. https://doi.org/10.1029/2019GL084199
- Fejer, B. G., & Kelley, M. C. (1980). Ionospheric irregularities. *Reviews of Geophysics*, 18(2), 401–454. https://doi.org/10.1029/RG018i002p00401 Fejer, B. G., Scherliess, L., & de Paula, E. R. (1999). Effects of the vertical plasma drift velocity on the generation and evolution of equatorial spread F. *Journal of Geophysical Research*, 104(A9), 19859–19869. https://doi.org/10.1029/1999ja900271
- Gentile, L. C., Burke, W. J., & Rich, F. J. (2006). A climatology of equatorial plasma bubbles from DMSP 1989-2004. Radio Science, 41(5), RS5S21, https://doi.org/10.1029/2005RS003340
- Gentile, L. C., Burke, W. J., Roddy, P. A., Retterer, J. M., & Tsunoda, R. T. (2011). Climatology of plasma density depletions observed by DMSP in the dawn sector. *Journal of Geophysical Research*, 116(A3), A03321. https://doi.org/10.1029/2010JA016176
- GIRO. (2023). Ionogram Data from global digisonde network. Access date 12 April 2023 Retrieved from https://hpde.io/SMWG/Observatory/GIRO GMT. (2023). Generic mapping tool software. Access date 12 April 2023 Retrieved from https://www.generic-mapping-tools.org/download/ GOLD. (2023). GOLD UV data: L1C NI1 product. Access date 12 April 2023 Retrieved from https://gold.cs.ucf.edu/data/
- Heelis, R. A., Stoneback, R. A., Perdue, M. D., Depew, M. D., Morgan, W. A., Mankey, M. W., et al. (2017). Ion velocity measurements for the ionospheric connections explorer. Space Science Reviews, 212(1–2), 615–629. https://doi.org/10.1007/s11214-017-0383-3
- Huang, C., De La Beaujardiére, O., Roddy, P. A., Hunton, D. E., Liu, J. Y., & Chen, S. P. (2014). Occurrence probability and amplitude of equatorial ionospheric irregularities associated with plasma bubbles during low and moderate solar activities (2008–2012). *Journal of Geophysical Research: Space Physics*, 119(2), 1186–1199. https://doi.org/10.1002/2013JA019212
- Huang, C. S., Beaujardiere, O. D. L., Roddy, P. A., Hunton, D. E., Pfaff, R. F., Valladares, C. E., & Ballenthin, J. O. (2011). Evolution of equatorial ionospheric plasma bubbles and formation of broad plasma depletions measured by the C/NOFS satellite during deep solar minimum. Journal of Geophysical Research, 116, A03309. https://doi.org/10.1029/2010JA015982
- Huang, C. Y., Burke, W. J., Machuzak, J. S., Gentile, L. C., & Sultan, P. J. (2001). DMSP observations of equatorial plasma bubbles in the topside ionosphere near solar maximum. *Journal of Geophysical Research*, 106(A5), 8131–8142. https://doi.org/10.1029/2000ja000319
- Huang, X., & Reinisch, B. W. (1996). Vertical electron density profiles from the digisonde network. Advances in Space Research, 18(6), 121–129. https://doi.org/10.1016/0273-1177(95)00912-4
- Hysell, D. L. (2000). An overview and synthesis of plasma irregularities in equatorial spread F. *Journal of Atmospheric and Solar-Terrestrial Physics*, 62(12), 1037–1056. https://doi.org/10.1016/s1364-6826(00)00095-x
- Hysell, D. L., & Burcham, J. D. (2002). Long term studies of equatorial spread F using the JULIA radar at Jicamarca. *Journal of Atmospheric and Solar-Terrestrial Physics*, 64(12–14), 1531–1543, https://doi.org/10.1016/S1364-6826(02)00091-3
- Joshi, D. R., Groves, K. M., Retterer, J. M., Carrano, C. S., & Roddy, P. A. (2022). Peak-height distribution of equatorial ionospheric plasma bubbles: Analysis and modeling of C/NOFS satellite observations. *Journal of Geophysical Research: Space Physics*, 127(9), e2022JA030525. https://doi.org/10.1029/2022JA030525
- Kelley, M. C. (1985). Equatorial spread F: Recent results and outstanding problems. *Journal of Atmospheric and Solar-Terrestrial Physics*, 47(8–10), 745–752. https://doi.org/10.1016/0021-9169(85)90051-0
- Kil, H. (2015). The morphology of equatorial plasma bubbles A review. Journal of Astronomy and Space Sciences, 32(1), 13–19. https://doi.org/10.5140/JASS.2015.32.1.13
- Kil, H., & Heelis, R. A. (1998). Global distribution of density irregularities in the equatorial ionosphere. *Journal of Geophysical Research*, 103(A1), 407–417. https://doi.org/10.1029/97ja02698
- Kil, H., Paxton, L. J., & Oh, S. J. (2009). Global bubble distribution seen from ROCSAT-1 and its association with the evening prereversal enhancement. *Journal of Geophysical Research*, 114(6), 1–9. https://doi.org/10.1029/2008JA013672

ZAKHARENKOVA ET AL. 15 of 16

- Kintner, P. M., Ledvina, B. M., De Paula, E. R., & Kantor, I. J. (2004). Size, shape, orientation, speed, and duration of GPS equatorial anomaly scintillations. *Radio Science*, 39(2). https://doi.org/10.1029/2003rs002878
- Liu, J., Chen, S., Yeh, W., Tsai, H., & Rajesh, P. (2016). Worst-case GPS scintillations on the ground estimated from radio occultation observations of FORMOSAT-3/COSMIC during 2007–2014. Surveys in Geophysics, 37(4), 791–809. https://doi.org/10.1007/s10712-015-9355-x
- Makela, J. J., Vadas, S. L., Muryanto, R., Duly, T., & Crowley, G. (2010). Periodic spacing between consecutive equatorial plasma bubbles. Geophysical Research Letters. 37(14), 1–5. https://doi.org/10.1029/2010GL043968
- Maruyama, T., & Matuura, N. (1984). Longitudinal variability of annual changes in activity of equatorial spread F and plasma bubbles. *Journal of Geophysical Research*, 89(A12), 10903–10912. https://doi.org/10.1029/JA089iA12p10903
- Nishioka, M., Basu, S., Basu, S., Valladares, C. E., Sheehan, R. E., Roddy, P. A., & Groves, K. M. (2011). C/NOFS satellite observations of equatorial ionospheric plasma structures supported by multiple ground based diagnostics in October 2008. *Journal of Geophysical Research*, 116(A10), A10323, https://doi.org/10.1029/2011JA016446
- Ossakow, S. L. (1981). Spread F theories: A review. Journal of Atmospheric and Terrestrial Physics, 43(5-6), 437-452. https://doi.org/10.1016/0021-9169(81)90107-0
- Pradipta, R., Valladares, C. E., & Doherty, P. H. (2015). An effective TEC data detrending method for the study of equatorial plasma bubbles and traveling ionospheric disturbances. *Journal of Geophysical Research: Space Physics*, 120(12), 11048–11055. https://doi. org/10.1002/2015JA021723
- Richmond, A. D. (1995). Ionospheric electrodynamics using magnetic apex coordinates. *Journal of Geomagnetism and Geoelectricity*, 47(2), 191–212, https://doi.org/10.5636/jgg.47.191
- SAO. (2023). SAO Explorer tool for interactive ionogram scaling. Access date 12 April 2023 Retrieved from https://ulcar.uml.edu/SAO-X/SAO-X.html
- Sokolovskiy, S., Schreiner, W., Rocken, C., & Hunt, D. (2002). Detection of high-altitude ionospheric irregularities with GPS/MET. *Geophysical Research Letters*, 29(3), 1033. https://doi.org/10.1029/2001GL013398
- Su, S. Y., Liu, C. H., Ho, H. H., & Chao, C. K. (2006). Distribution characteristics of topside ionospheric density irregularities: Equatorial versus midlatitude regions. *Journal of Geophysical Research*, 111(6), A06305, https://doi.org/10.1029/2005JA011330
- Tsunoda, R. T. (1983). On the generation and growth of equatorial backscatter plumes: 2. Structuring of the west walls of upwellings. *Journal of Geophysical Research*, 88(A6), 4869. https://doi.org/10.1029/JA088iA06p04869
- Tsunoda, R. T., Bubenik, D. M., Thampi, S. V., & Yamamoto, M. (2010). On large-scale wave structure and equatorial spread F without a post-sunset rise of the F layer. *Geophysical Research Letters*, 37(7), L07105. https://doi.org/10.1029/2009g1042357
- Tsunoda, R. T., Livingston, R. C., McClure, J. P., & Hanson, W. B. (1982). Equatorial plasma bubbles: Vertically elongated wedges from the bottomside F layer. *Journal of Geophysical Research*, 87(A11), 9171. https://doi.org/10.1029/ja087ia11p09171
- UCAR COSMIC Program. (2019). COSMIC-2 data products: IVM in situ density. UCAR/NCAR—COSMIC. Access date 12 April 2023. https://doi.org/10.5065/T353-C093
- Valladares, C. E., Sheehan, R., Basu, S., Kuenzler, H., & Espinoza, J. (1996). The multi-instrumented studies of equatorial thermosphere aeronomy scintillation system: Climatology of zonal drifts. *Journal of Geophysical Research*, 101(A12), 26839–26850. https://doi.
- org/10.1029/96JA00183

 Watson, C., & Pedatella, N. M. (2018). Climatology and characteristics of medium-scale F region ionospheric plasma irregularities observed by COSMIC radio occultation receivers. *Journal of Geophysical Research: Space Physics*, 123(10), 8610–8630. https://doi.
- org/10.1029/2018JA025696
 Wessel, P., Smith, W. H., Scharroo, R., Luis, J., & Wobbe, F. (2013). Generic mapping tools: Improved version released. *Eos, Transactions American Geophysical Union*, 94(45), 409–410. https://doi.org/10.1002/2013EO450001
- Woodman, R. F., & La Hoz, C. (1976). Radar observations of F region equatorial irregularities. *Journal of Geophysical Research*, 81(31), 5447–5466. https://doi.org/10.1029/ja081i031p05447
- Wu, Q., Pedatella, N. M., Braun, J. J., Schreiner, W., Weiss, J., Chou, M.-Y., et al. (2022). Comparisons of ion density from IVM with the GNSS differential TEC-derived electron density on the FORMOSAT-7/COSMIC-2 mission. *Journal of Geophysical Research: Space Physics*, 127(8), e2022JA030392. https://doi.org/10.1029/2022JA030392
- Xiong, C., Park, J., Lühr, H., Stolle, C., & Ma, S. Y. (2010). Comparing plasma bubble occurrence rates at CHAMP and GRACE altitudes during high and low solar activity. *Annales Geophysicae*, 28(9), 1647–1658. https://doi.org/10.5194/angeo-28-1647-2010
- Yizengaw, E., Retterer, J., Pacheco, E. E., Roddy, P., Groves, K., Caton, R., & Baki, P. (2013). Postmidnight bubbles and scintillations in the quiet-time June solstice. Geophysical Research Letters, 40(21), 5592–5597. https://doi.org/10.1002/2013GL058307
- Yue, X., Schreiner, W. S., Pedatella, N. M., & Kuo, Y.-H. (2016). Characterizing GPS radio occultation loss of lock due to ionospheric weather. Space Weather, 14(4), 285–299. https://doi.org/10.1002/2015SW001340
- Zakharenkova, I., Astafyeva, E., & Cherniak, I. (2016). GPS and in situ Swarm observations of the equatorial plasma density irregularities in the topside ionosphere. Earth Planets and Space, 68(1), 120. https://doi.org/10.1186/s40623-016-0490-5

ZAKHARENKOVA ET AL. 16 of 16